Cloud-Top Properties of Growing Cumulus prior to Convective Initiation as Measured by Meteosat Second Generation. Part I: Infrared Fields

John R. Mecikalski

Atmospheric Science Department, University of Alabama in Huntsville, Huntsville, Alabama

Wayne M. MacKenzie Jr.

Earth Systems Science Center, University of Alabama in Huntsville, Huntsville, Alabama

Marianne Koenig

European Organisation for the Exploitation of Meteorological Satellites, Darmstadt, Germany

Sam Muller

Jupiter's Call, LLC, Madison, Alabama

(Manuscript received 15 July 2009, in final form 22 September 2009)

ABSTRACT

Infrared (IR) data from the Meteosat Second Generation (MSG) satellite are used to understand cloud-top signatures for growing cumulus clouds prior to known convective initiation (CI) events, or the first occurrence of a $\geq$35-dBZ echo from a new convective cloud. In the process, this study proposes how MSG IR fields may be used to infer three physical attributes of growing cumuli, cloud depth, cloud-top glaciation, and updraft strength, with limited information redundancy. These three aspects are observed as unique signatures within MSG IR data, for which this study seeks to relate to previous research, as well as develop a new understanding on which subset of IR information best identifies these attributes. Data from 123 subjectively identified CI events observed during the 2007 Convection and Orographically Induced Precipitation Study (COPS) field experiment conducted over southern Germany and northeastern France are processed, per convective cell, to meet this study's objectives. A total of 67 IR ''interest fields'' are initially assessed for growing cumulus clouds, with correlation and principal component analyses used to highlight the top 21 fields that are considered the best candidates for describing the three attributes. Using between 6 and 8 fields per category, a method is then proposed on how growing convective clouds may be quantified per 3-km^2 pixel (or per cumulus cloud object) toward inferring each attribute. No independent CI-nowcasting analysis is performed, which instead is the subject of ongoing research.

1. Introduction

The algorithm of Mecikalski and Bedka (2006), which is referred to as the Satellite Convection Analysis and Tracking (SATCAST) system, demonstrates how the spatial, temporal, and spectral information from the Geostationary Operational Environmental Satellite (GOES; Menzel et al. 1998) meteorological satellite data can be used collectively to identify, track, and monitor growing convective clouds in their preconvective initiation state, to nowcast (0–1-h forecast) convective intiation (CI). Here, CI is formally defined as the first occurrence of a $\geq$35-dBZ radar echo at the lowest elevation tilt (see also Weckwerth and Parsons 2006). SATCAST and other convective nowcasting algorithms rely on a sound understanding of how to relate infrared (IR) information (as collected by spaceborne instruments) to attributes of growing convective clouds. Subsequently, cloud attributes (as described below) can be related to in-cloud processes, which help to determine the future growth potential and evolution of these clouds.

Corresponding author address: John R. Mecikalski, Atmospheric Science Dept., University of Alabama in Huntsville, NSSTC, 320 Sparkman Dr., Huntsville, AL 35805-1912.
E-mail: john.mecikalski@nsstc.uah.edu

Use of GOES data has shown promise relating four IR fields to the CI process. Several current and certainly forthcoming geostationary imagers provide at least double the amount of IR channels, at 3–4-km resolution. Therefore, developing an understanding that guides the proper use of the "new" IR channel information to improve applications such as CI nowcasting will be needed. This requires that basic research be done so that the information in the IR of growing cumulus clouds can be related to and help us understand physical processes known to precede CI. One such instrument that can play a role in this understanding is the Spinning Enhanced Visible and Infrared Imager (SEVIRI) that is aboard the Meteosat Second Generation (MSG) meteorological satellite, as centered over the equator at 0° longitude (Schmetz et al. 2002). SEVIRI affords an opportunity to learn how eight IR channels may be used to examine the CI process through cloud-top property analysis. Of note, the GOES sounder possesses 18 IR and 1 visible channel, and it has a field-of-view sampling of 10 km at the subsatellite point, near 14 km over the continental United States, which is too high for adequately estimating cumulus cloud growth that occurs mainly on 1–4-km scales.

Therefore, the goals of this study are the following: 1) to extend our understanding on how various information in the IR spectrum may be used to monitor physical attributes and inferred processes within new cumulus clouds, relating IR cloud-top observations to aspects of cumulus clouds prior to CI, and 2) to evaluate the most useful subset of channel combinations and derived fields (from the eight SEVIRI IR channels) that best describe the important aspects of developing cumuli. These aspects include in-cloud updraft magnitude, updraft width, cloud depth, and especially cloud-top phase transition (or glaciation). All of these vary as a function of convective cloud evolution (Browning and Atlas 1965; Bethwaite et al. 1966; Balaji and Clark 1988; Ziegler et al. 1997); because they can be monitored on 5–30-min time intervals by geostationary satellites, the ability to forecast CI may be improved significantly if we understand how to interpret satellite signatures of growing cumulus clouds. Because of these goals and how the study was conducted, via the human-expert analysis of known CI events without the development of an independent testing dataset, this paper cannot cover aspects of validation and skill score analysis of a specific nowcasting algorithm. The issue of assessing the most important IR fields for estimating CI potential also cannot be addressed by this study because it requires the formulation of a significantly large dataset, complete with null cases, which is the subject of ongoing research. Part two of this study will perform a similar analysis to what is presented here on SEVIRI's visible and reflectance fields.

This paper proceeds as follows: Section 2 provides a background on previous research that relates geostationary satellite data to developing cumulus clouds and the CI nowcasting problem, the motivation for this type of research. Section 3 overviews the MSG datasets used for this study and how they were processed. In section 3, the information specific to the 2007 Convection and Orograpically Induced Precipitation Study (COPS) field experiment are provided because it was over the region (southern Germany and northeastern France) where CI events were identified and MSG data were analyzed. Section 4 presents the results. The main conclusions are discussed and the paper is concluded in section 5.

2. Background

Forecasting the initiation of atmospheric convection remains a significant challenge today for two main reasons. 1) The processes that dictate when and where thunderstorms first form on a given day because of solar heating are very often poorly resolved by numerical weather prediction (NWP) models (e.g., Zhang et al. 2006). 2) The observational data needed to assess the conditions leading up to CI are significantly lacking, absent entirely, or (if present) not available on the space and time scales needed to monitor elements such as the strength of the capping inversion, boundary layer moisture and mass convergence, and low-level thermodynamic character (e.g., equivalent potential temperature θ_e; see Browning 1982; Wilson et al. 1998; Jacobs and Maat 2005). One approach that has shown promise for identifying new CI events involves processing geostationary satellite data and linearly extrapolating information on developing cumulus clouds (Mecikalski and Bedka 2006; Mecikalski et al. 2007). CI forecast lead times are increased from ~10 to 75 min as a result of pure extrapolation, depending on the environment. Geostationary imagery, especially in the near-IR (NIR) and IR spectrum (3.7–13.5 μm), has been processed for nearly two decades in the identification of cloud types (Baum et al. 1997; Berendes et al. 1999, 2008), cloud motion (Sadler and Kilonsky 1985; Velden et al. 1997), cloud-top properties (Nair et al. 1998; Goloub et al. 2000; Baum et al. 2000a,b; Baum and Spinhirne 2000), and cloud evolution (e.g., Rickenbach et al. 2008). With spatial resolutions in the 1–4-km range, these data are ideal for identifying and monitoring convective scales, whereas the temporal resolutions of 5–15 min measure rapid changes in convective cloud evolution, appropriate for these phenomena.

For understanding CI using geostationary satellite data, well-established and robust methods are in existence, which exploit data from MSG, GOES, the Multifunctional

Transport Satellite (MTSAT), and eventually the forthcoming high-spectral-resolution data (e.g., the Meteosat Third Generation Infrared Sounder). Several of these methods capitalize on the combined use of NWP and IR observations. For example, the work by Zinner et al. (2008) has shown that convection can be identified across scales so that thunderstorms and mesoscale convective systems can be monitored as they travel, largely relying on geostationary imagery from MSG. Rosenfeld et al. (2008), McCann (1983), Levizzani and Setvák (1996), Setvák et al. (2003), and Brunner et al. (2007) have demonstrated how data from MSG and GOES may be used to evaluate convective storm intensity; enhance "V" signatures; and exploit 3.9-μm reflectance information as a means of estimating the effective radii of frozen hydrometeors and relating this back to updraft intensity (e.g., strong updrafts cause rapid freezing before substantial hydrometeor growth, and mostly small-sized ice crystals; Rosenfeld et al. 2008). The AutoNowcaster (Mueller et al. 1993, 2003) is another example of a thunderstorm nowcast system that combines satellite and NWP data toward nowcasting CI and subsequently monitoring storm evolution and motion. Understanding how to utilize satellite data efficiently should improve our ability to predict a new storm development within such systems.

Previous satellite studies that glean an understanding of convective clouds have effectively highlighted how GOES (Purdom 1976, 1982; Adler et al. 1985; Mecikalski and Bedka 2006; Mecikalski et al. 2008) and MSG (Rosenfeld et al. 2008; Lensky and Rosenfeld 2008) can be used to describe the physical attributes occurring in developing cumulus clouds. These physical attributes are the following: 1) in-cloud updraft strength (an inferred physical process); 2) cumulus cloud width (i.e., updraft width) and feature expansion; 3) cloud depth (i.e., the height of the updraft); 4) and cloud-top glaciation (and inferred microphysical processes). This analysis is built around an understanding of these attributes and in-cloud processes, which will guide the interpretation of the results.

In terms of cumulus cloud behaviors related specifically to *GOES-12* IR information, previous research (Mecikalski and Bedka 2006) suggests the following: 1) The 8-km resolution 13.3-μm channel fortuitously aids in detecting and observing cloud growth of the wider, larger cumulus clouds (i.e. wide updrafts provide high brightness temperature T_B signatures in 8-km data); however, higher-resolution data ($\leq$1 km) are always desired, because one can gain a better sense of the updraft width using $\sim$11-μm T_B gradient-based methods. 2) Colder cloud-top T_B values are associated with cumuli more likely to begin producing heavy precipitation. 3) The 6.5–10.7-μm T_B difference indicates cumuli

growing into midtropospheric levels (especially at small view angles) where the weighting functions of these two channels become superimposed, implying that a capping inversion may no longer be present. 4) The time trends in 6.5–10.7- and 13.3–10.7-μm T_B differences measure the rate of convective cloud growth, or depth changes. The 15- and 30-min cloud-top cooling rates measured through 10.7-μm T_B values are quite important as well for estimating cumulus growth (Roberts and Rutledge 2003), because they are indicators of in-cloud updraft strength (see Adler and Fenn 1979). Recent work shows how GOES data via the SATCAST algorithm can also be used to monitor nighttime CI, as well as first-time lightning initiation, exploiting 3.9-μm channel data (emitted T_B and fractional reflectance; see also Lindsey et al. 2006). Mecikalski et al. (2008) highlight the need to understand when certain IR fields contain redundant information on cumulus cloud-top attributes as compared to other IR fields, which is a goal of this study for SEVIRI IR data. The data and processing methodology are described in the next section, followed by our main results.

3. Data processing methodology

a. MSG imagery and interest fields

The main dataset for this project is calibrated level-1.5 IR channels collected at a 3-km sampling distance from the SEVIRI instrument on the MSG (specifically *Meteosat-9*) satellite as located over the equator at 0° longitude. The subsatellite sampling distance is 3 km, whereas data resolution over the COPS region is >3 km because of the view angle. The SEVIRI instrument possesses eight IR channels, with central wavelengths of 3.9, 6.2, 7.3, 8.7, 9.7, 10.8, 12.0, and 13.4 μm; one NIR 1.6-μm channel; two visible wavelengths centered on 0.6 and 0.8 μm; and one high-resolution visible channel (HRV; Schmetz et al. 2002). The HRV data possess a 1-km sampling distance at the subsatellite point (see EUMETSAT 2007). The use of the visible data, including the reflected component of the 3.9-μm channel, will be treated separately in part two of this study. HRV data were used here only to help evaluate towering cumulus fields, to corroborate the IR data analysis, and were not processed further. Data at time intervals of 15 min were used. Although 5-min "rapid scan" data were available during a portion of COPS 2007 from MSG, previous CI research utilizes 15-min time-trend fields; therefore, the decision was made to mimic past work.

From the MSG channels, using techniques outlined in Mecikalski and Bedka (2006) and Mecikalski et al. (2008), 67 separate so-called IR interest fields for CI, or

simply "interest fields," are evaluated. In many cases, previous studies have documented the importance of a given interest field, and in these cases the reference is provided.

b. COPS 2007

All *Meteosat-9* data used in the study were collected for CI events observed during the COPS 2007 campaign (Wulfmeyer et al. 2008), which was conducted over southern Germany and northeast France from 4 June to 31 August 2007 (available online at http://www.cops2007.de). The geographical domain over which data were processed was 46.5°–49.0°N, 6.5°–11.0°E.

One main scientific goal driving COPS was to increase the understanding of CI as induced, in part, by orography (Wulfmeyer et al. 2008); therefore, a host of observational data were collected and archived. Two datasets in addition to MSG data were used from this COPS archive: soundings considered when performing parallax corrections (collected by the Institut für Meteorologie und Klimforschung at the Universität Karlsruhe) and dual-polarimetric radar collected in Waltenheim-sur-Zorn (48.739 75°N, 7.610 33°E) by the Monostatic Polarimetric Diversity Doppler Radar System (POLDIRAD), operated by the Deutsches Zentrum für Luft- und Raumfahrt (DLR), Institut für Physik der Atmosphäre. Data from several other radars operating over the COPS domain were used similarly (Karlsruhe, Rhine Valley supersite, and Vosges Mountains supersite).

c. CI event identification

Of the 88 COPS data collection days, 26 were evaluated because they possessed active CI. Further analysis revealed that 15 days possessed CI events occurring in conditions unobscured by higher clouds, such that new cumulus could be observed by *Meteosat-9*. Table 1 presents the COPS days analyzed, the times on each day over which data were collected, and the number of storms specifically identified. All storms were identified by a human expert in channel 9 (10.8 μm) and HRV data. A "good quality" event is defined as cumulus clouds that are developing in mostly clear-sky conditions over a 30-min time period preceding CI, then 15–45 min into the future without "interference" from high-level cirrus, which can lead to false identification. For the 15 days, all 15-min imagery were gathered (Table 1), and a subset domain was analyzed from the 3712 × 3712 IR and 5568 × 11136 HRV full-disk data. This amounted to processing IR images of 131 elements by 61 lines and HRV images of 393 × 183, covering the COPS domain.

Figures 1a–d exemplifies a COPS CI event, with the cumuli in various stages of development that are not obscured by higher clouds. Figures 2a–d shows a similar

TABLE 1. The COPS 2007 CI days used in this study, with time range and number of CI events per day.

Date	CI times	CI events
4 Jun	1142–1557 UTC	12
5 Jun	1057–1642 UTC	13
8 Jun	0942–1612 UTC	15
9 Jun	0927–1457 UTC	6
10 Jun	0812–0957 UTC	8
11 Jun	1012–1757 UTC	15
22 Jun	1342–1627 UTC	4
23 Jun	1042–1342 UTC	8
12 Jul	1327–1357 UTC	2
20 Jul	942–1827 UTC	14
21 Jul	1527–1742 UTC	4
24 Jul	1257–1712 UTC	6
28 Jul	1457–1812 UTC	7
2 Aug	1242–1857 UTC	3
3 Aug	1242–1657 UTC	6
Total		123

example (not for the clouds in Fig. 1) in 10.8-μm data, with a square surrounding the cell undergoing CI over the 30-min time frame, and the POLDIRAD radar image (Fig. 2d) 30 min later than the image shown in Fig. 2c. In our processing, the three MSG images would ideally be gathered in this order: first, for conditions in Fig. 1a; next, when the cumulus clouds were at the growth stage of Fig. 1b; and third, the last coincident with Fig. 1c. By Fig. 1d (between 15–45 min after Fig. 1c), a radar echo would first be observed. However, over the 123 events studies, it is likely that for a few cases a ≥35-dBZ echo was present by the third image time in the sequence. We feel that these cases still capture the main aspects of cumulus cloud development as viewed by IR channel information, especially given the consistency of the results obtained.

The method of convective cell tracking involved manually observing towering cumuli that evolved over three successive 15-min images into a large cumulus cloud (cumulus congestus and cumulonimbus) or a cloud that clearly possessed a new anvil. Data from the POLDIRAD and other radars were viewed in their native resolution as a means of confirming CI, and for this study radar reflectivity simply had to be ≥35 dBZ to be classified as a CI event. It is important to note that the actual dBZ value at or above 35 that occurred with a given new storm was not recorded, which would be important for studies interested in determining relationships between IR cloud properties and rainfall intensity (e.g., Scofield 1987; Rozumalski 2000).

d. IR field analysis

1) PHYSICAL ATTRIBUTE REPRESENTATION

The analysis and results below are built around an understanding of the four physical attributes (and inferred in-cloud processes) listed, which will subsequently guide
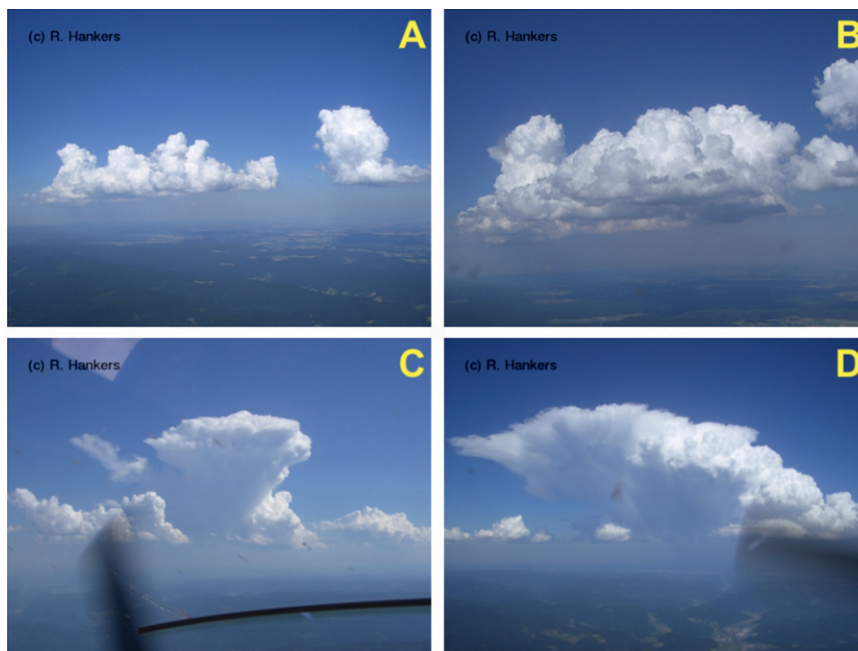
FIG. 1. A CI event as viewed by aircraft during COPS (images courtesy of R. Hankers and available online at http://www.cops2007.de). Cumulus are shown in several stages of development, from (a) ''fair weather'' or mediocris (moderate), (b),(c) to congestus or towering, (d) to newly glaciated (cumulonimbus calvus) with no obvious rainfall reaching the ground. Image artifacts in (c) and (d) are caused by propellers' blades, reflections off the aircraft window, and insects on the aircraft window.

the interpretation of results. With 67 IR interest fields available, the motivation of our analysis (in this order) is toward the following:

1) determining uniqueness within the data;
2) removing redundant fields;
3) relating all fields to relevant processes occurring in cumulus clouds undergoing CI; and
4) forming a substantially more limited subset of the 67 fields, determining a list of the best, nonredundant candidate fields for describing each of the three main categories of cumulus cloud behavior: cloud depth, updraft strength, and cloud-top glaciation.

Cloud width (i.e., updraft width) and feature expansion are also important attributes of new convective clouds that can be monitored by geostationary imagery; however, they are quantified better in data with sampling distances <3 km (i.e., in ≤1-km visible data), given the small scales involved.

2) REDUCTION AND REDUNDANCY

As a means of accomplishing 1 and 2 from the study's motivation list, the following procedures were used: A 67×67 correlation matrix was formed and analyzed. Fields were then grouped according to the physical process they estimate, as shown in Tables 2–4. Within

the categories, cases with field-to-field cross correlations of >0.80 were highlighted. When done, an assessment was made toward identifying multiple, high cross correlations between three or more fields. The result was the removal of numerous fields that contained redundant information on a given physical attribute. For example, for the fields that describe cumulus cloud depth, cross correlations >0.80 were found between the 10.8-μm T_B, the 13.4–10.8-μm difference, the 7.3–10.8-μm difference, the 8.7–10.8-μm difference, the 8.7–13.4-μm difference, the 6.2–10.8-μm difference, and the 6.2–7.3-μm difference. Given that previous CI nowcasting methods already rely on the 10.8-μm T_B and that the only other field in this list to not contain 10.8-μm T_B is the 6.2–7.3-μm channel difference, these two were retained. The same process was performed for the cloud-top glaciation (Table 3) and updraft strength field (Table 4) groups.

The correlation analysis revealed other redundant aspects within the 67 IR fields. Specifically, many of the fields with unknown ''critical values,'' or unknown physical meaning with respect to growing cumulus clouds, often effectively duplicated fields with more interpretation (based on previous research). Specifically from Table 2, the channel differences 6.2–12.0, 6.2–13.4, 7.3–10.8, 7.3–12.0, 7.3–13.4, 8.7–12.0, 8.7–13.4, and 8.7–7.3 μm and most
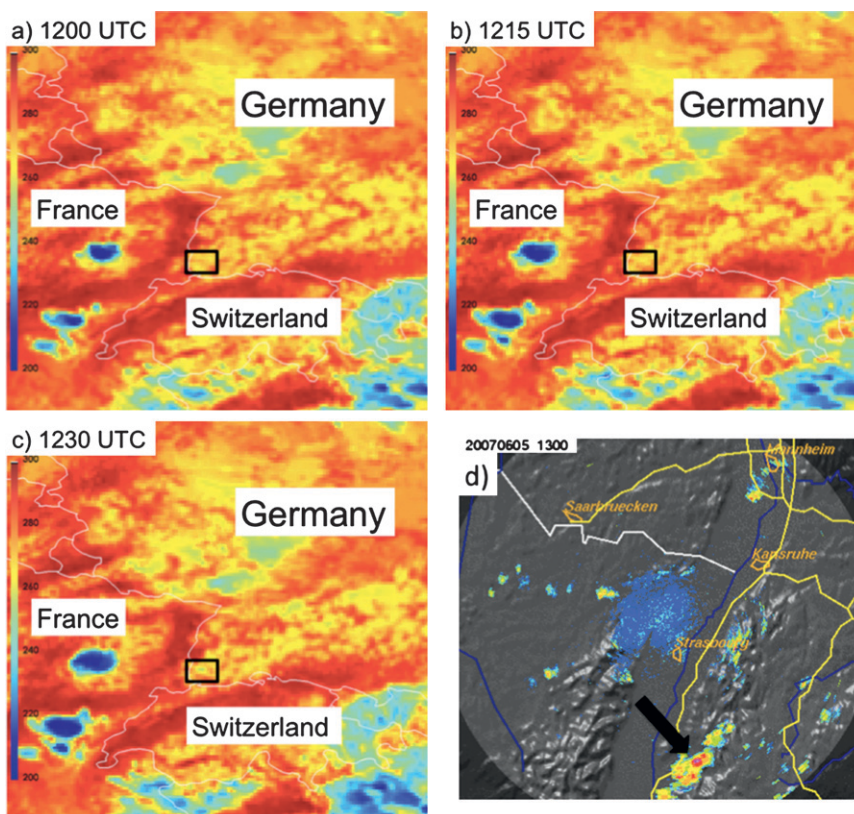
FIG. 2. (a)–(c) An example of one CI event as processed in SEVIRI 10.8-μm data, with (d) a radar image. The squares in (a)–(c) highlight small regions where cumulus clouds were forming as they moved over a 30-min time frame, from 1200 to 1230 UTC, prior to CI for this sequence. In (d), the radar image, from the POLDIRAD site at 1300 UTC, shows the lowest scan reflectivity associated with the developing cumulus clouds in (a)–(c). A total of 123 such image sets, often with multiple CI events occurring within an image, were processed for this study.

differences involving the 9.7 μm channel behaved similarly as cumuli deepened. The time trends of these differences were also highly correlated. Therefore, when seeking to reduce the number of IR fields for describing cloud depth and updraft strength, the decision was made to remove those fields where 1) further research would be required to discern the physical meaning of a field's spectral information with respect to cumulus growth; 2) the use of a particular channel was not necessarily appropriate for describing growing clouds because of point 1, and the channel was never intended for convective cloud analysis (e.g., 9.7 μm is used mainly for ozone detection); and/or 3) a given channel difference for which significant research had been previously performed, to understand its value in cumulus cloud analysis, could be used in place of others [e.g., using the 6.2–10.8-μm (Ackerman 1996) difference versus the 6.2–12.0-μm difference and associated time trends].

In the case of cloud-top glaciation, only a few fields were significantly highly correlated. They included the 15- and 30-min trispectral difference [(8.7–10.8) − (10.8–12.0) μm; Strabala et al. 1994], the 15- and 30-min 3.9–10.8-μm trends (Ellrod 1995), the 15- and 30-min 10.8–12.0-μm trends (Inoue 1987a,b; Prata 1989; Strabala et al. 1994; Holz et al. 2006; see also Pavolonis et al. 2006), the 13.4–10.8-μm difference (see Ellrod 2004), and trends of the 8.7–10.8-μm difference (Ackerman et al. 1992). Surprisingly, many of these time trends were not correlated much above 0.70. This suggests that the relationships between variables describing cloud-top glaciation are somewhat nonlinear, whereas the trends nicely behave temporally, varying across clouds in different environments (from day to day) and/or possessing a wide range of spectral signatures, likely a function of updraft velocity (Lensky and Rosenfeld 2008; Rosenfeld et al. 2008).

When substantial cross correlation exists (>0.80), it is likely that substitute fields could be used in place of traditional channel data. Hypothetically, if the 10.8-μm channel on *Meteosat-9* was not available, it is expected

TABLE 2. *Meteosat-9* IR interest fields to be evaluated for 0–1-h CI nowcasting that describe cloud depth or the change in cumulus cloud depth with time. The number of fields developed from a given CI interest field is listed in the middle column. Notes are included when a previous study has performed research related to a given Interest Field, or to list other pertinent information.

Interest fields	No. of fields	Critical value[a]
Cloud depth indicators		
10.8-μm T_B	1	<0°C
6.2–10.8 μm	1	From −30° to −10°C[b]
6.2–12.0 μm	1	Unknown
6.2–13.4 μm	1	Unknown
7.3–10.8 μm	1	Unknown
7.3–12.0 μm	1	Unknown
7.3–13.4 μm	1	Unknown
13.4–10.8 μm	1	From −25° to −5°C[c]
8.7–12.0 μm	1	Unknown
8.7–13.4 μm	1	Unknown
9.7–10.8 μm	1	Unknown
9.7–12.0 μm	1	Unknown
9.7–13.4 μm	1	Unknown
6.2–9.7 μm	1	Differences toward 0
7.3–9.7 μm	1	Differences toward 0
8.7–9.7 μm	1	Differences toward 0
8.7–7.3 μm	1	Differences toward 0
6.2–7.3 μm	1	Differences toward 0
Total fields	18	

[a] If available from previous research.
[b] Ackerman (1996) and Schmetz et al. (1997).
[c] Mecikalski and Bedka (2006).

TABLE 3. As in Table 2, but for IR interest fields that describe cumulus cloud-top glaciation.

Interest fields	No. of fields	Critical value[a]
Glaciation indicators		
Freeze transition (10.8-μm T_B)	1	Drops below 0°C over previous 30 min
3.9–10.8 μm and time trends[b]	3	>|−5|°C Transition across 0°C[c]
8.7–10.8 μm and time trends	3	<0°C for nontrends[d]
(8.7–10.8)–(10.8–12.0) μm	1	Becoming >0°[e]
12.0–10.8 μm	1	>1°C (15 min)$^{-1}$[f]
Trispectral time trends	2	Positive trends
Total fields	11	

[a] If available from previous research.
[b] Two time trends are considered, 15 and 30 min.
[c] Time trends value.
[d] Ackerman et al. (1992) and Strabala et al. (1994).
[e] "Tri-spectral" method; see Strabala et al. (1994) and Baum et al. (2000b).
[f] Ellrod (1995).

based on these analyses that the 6.2–12.0-μm field could be used instead or in place of the 6.2–10.8-μm difference. Should users of this study's results wish to "overfit" the problem of assessing cloud depth and/or updraft strength of cumuli using MSG IR data, then using all 67 fields, despite the redundancy, would accomplish that goal. More will be said on this in the results section.

Once three groups, each containing a smaller number of fields, were obtained, principal component analysis (PCA; Johnson and Wichern 2002) was performed. The goal of using PCA is to help further quantify field redundancy to establish a short list of candidate fields for describing substantial cumulus cloud development. Given that the units of all interest fields were either T_B or the change in T_B, PCA using the correlation matrix was performed, which normalizes the data to the same magnitudes; without this step, fields with larger data magnitudes would show a spuriously high amount of the explained variance (ExpVar; Johnson and Wichern 2002).

4. Results

a. PCA

Tables 5–7 present the PCA results for the reduced set of IR fields that can be used to estimate cloud depth

(Table 5), cloud-top glaciation (Table 6), and updraft strength (Table 7). In these tables, ranking is determined from the size of the absolute value of the eigenvalues of the 6–8 fields. The size of the eigenvalues in principal component 1 and, if needed, component 2 from the PCA, provide the ranking information. This ranking may perhaps be used as a means of weighting each IR interest field in terms of importance when describing a given attribute or process, per *Meteosat-9* pixel or per cumulus cloud object; however, tests with an independent dataset complete with "null" cases would be required to establish field importance within each list.

In Table 5, the 6.2–10.8-μm (Schmetz et al. 1997) difference has the highest ranking when estimating cumulus cloud depth, with the 6.2–7.3-μm difference and 10.8-μm T_B as the second and third, respectively. Table 6 shows the top three fields as the 15-min trend in the trispectral difference [(8.7–10.8) − (10.8–12.0)], the instantaneous trispectral difference, followed by the 15-min 8.7–10.8-μm time trend, all physically consistent, well-documented indicators of cloud-top glaciation (Baum et al. 2000b). Table 7 shows that the 30-min 6.2–7.3-μm difference and the two time trends of 10.8-μm T_B (as in Roberts and Rutledge 2003) as highly ranked IR fields for estimating updraft strength and hence cumulus cloud growth rates in advance of CI.

An important point, in light of Figs. 1a–d and through use of PCA, is that, for establishing time trends and developing understanding between IR fields and cloud-top properties, our analysis takes a purely linear approach to the problem. PCA is a linear analysis technique that assumes similar relationships in the data and therefore how

TABLE 4. As in Table 2, but for IR interest fields that describe cumulus cloud updraft strength.

CI Interest fields	No. of fields	Critical value[a]
Updraft strength indicators		
10.8-μm T_B time trends[b]	2	$<-4°C$ (15 min)$^{-1}$ ΔT_B (30 min)$^{-1}$ $<\Delta T_B$ (15 min)$^{-1c}$
6.2–10.8-μm time trends	2	$>$2–3°C (15 min)$^{-1d}$
6.2–12.0-μm time trends	2	Unknown
6.2–13.4-μm time trends	2	Unknown
7.3–10.8-μm time trends	2	Unknown
7.3–12.0-μm time trends	2	Unknown
7.3–13.4-μm time trends	2	Unknown
12.0–10.8-μm time trends	2	$>$1°C (15 min)$^{-1e}$
13.4–10.8-μm time trends	2	$>$3°C (15 min)$^{-1f}$
8.7–12.0-μm time trends	2	Unknown
8.7–13.4-μm time trends	2	Unknown
9.7–10.8-μm time trends	2	Unknown
9.7–12.0-μm time trends	2	Unknown
9.7–13.4-μm time trends	2	Unknown
6.2–9.7-μm time trends	2	Positive trends
7.3–9.7-μm time trends	2	Positive trends
8.7–9.7-μm time trends	2	Positive trends
8.7–7.3-μm time trends	2	Positive trends
6.2–7.3-μm time trends	2	Positive trends
Total fields	38	

[a] If available from previous research.
[b] Two time trends are considered, 15 and 30 min.
[c] Roberts and Rutledge (2003).
[d] Ackerman (1996) and Schmetz et al. (1997).
[e] Prata (1989).
[f] Mecikalski and Bedka (2006).

IR properties change with cloud depth, updraft strength, and glaciation. However, it is recognized that as cumulus clouds grow in depth, nonlinear associations indeed exist. The approach of using three images in sequence therefore greatly simplifies, at times, more complicated relationships. The current version of the SATCAST algorithm was formed using 15-min temporal frequency GOES imagery, the most routinely available data, which also simplifies the problem of CI nowcasting using IR interest fields. Future work, using >3 images separated by 5-min time periods, will alleviate this shortcoming.

b. Physical explanation

For Tables 5–7, the cited literature highlights the physical interpretation of a given channel difference or time trend. In contrast, several fields not documented in the literature are shown to possess unique value when monitoring cumulus cloud growth and evolution. These include the following: 1) the 8.7–12.0-μm difference (Table 5), 2) the 6.2–7.3-μm difference (Table 5), 3) the 6.2–9.7-μm difference (Table 5), 4) the 7.3–13.4-μm difference (Table 5), 5) the 30-min 9.7–13.4-μm trend (Table 7), 6) the 15-min 7.3–9.7-μm trend (Table 7), 7) the 15-min 6.2–7.3-μm trend (Table 7), and 8) the 30-min 6.2–7.3-μm trend (Table 7). Toward the explaining of their relationship to cumulus cloud processes, Fig. 3 presents the clear-sky weighting functions for MSG (*Meteosat-9*) for each channel.

For channel differences in the previous list that are used to describe cloud depth, the implication is that, as cumuli grow, the T_B values associated with the specific weighting functions effectively become aligned at the same altitude; hence, the ΔT_B becomes small and near zero (or even slightly negative). This is particularly true for the 6.2- and 7.3-μm channels, which possess similarly shaped weighting functions, offset mostly in height. Certainly, local to regional variations in water vapor and temperature (and ozone for the 9.7-μm channel) between convective environments will alter the altitude of maximum response ("saturation") for a given channel. However, for a growing cumulus cloud, the previous statement should generally be true. For example, one could theoretically use the 6.2–7.3-, 7.3–8.7-, 8.7–9.7-, and 9.7–10.8-μm differences in successive order to estimate whether a convective cloud has grown to a given altitude. This can be extended to include the 12.0- and 13.4-μm channels as well, because both of these have been previously documented as important for estimating cloud-top height. Using these differences in this particular order and monitoring them as they become near zero implies a continuously growing and deepening cumulus cloud. Eventually, once a cloud extends to the

TABLE 5. PCA of the top 6 fields that describe cloud depth in IR MSG data. For this PCA, the correlation matrix was used and the cumulative proportion of the ExpVar is listed. Only the first four components are shown. A dash signifies an insignificant value (<0.100). The ranks of the fields to the assessment of cloud depth in this case are shown in the far-left column.

Rank	Interest fields	Component 1	Component 2	Component 3	Component 4
1	6.2–10.8 μm	−0.516	—	0.146	−0.106
2	6.2–7.3 μm	−0.503	—	0.271	−0.153
3	10.8-μm T_B	0.496	0.116	−0.367	—
4	7.3–13.4 μm	−0.385	—	−0.489	0.778
5	6.2–9.7 μm	−0.269	0.604	−0.560	−0.458
6	8.7–12.0 μm	−0.117	−0.786	−0.466	−0.387
	ExpVar	0.608	0.808	0.909	0.995

TABLE 6. As in Table 5, but the PCA of top 7 fields that describe cloud-top glaciation in IR MSG data. Here, the trispectral is (8.7–10.8)–(10.8–12.0) μm.

Rank	Interest fields	Component 1	Component 2	Component 3	Component 4
1	15-min trispectral	−0.477	—	0.282	0.361
2	Trispectral	−0.447	—	−0.508	−0.174
3	15-min 8.7–10.8 μm	−0.403	−0.413	0.145	0.317
4	8.7–10.8 μm	−0.383	−0.393	−0.437	−0.175
5	15-min 12.0–10.8 μm	−0.353	0.451	0.338	0.248
6	15-min 3.9–10.8 μm	−0.286	—	0.513	−0.802
7	12.0–10.8 μm	−0.239	0.677	−0.269	—
	ExpVar	0.518	0.720	0.854	0.954

tropopause or local equilibrium level, all differences will be near zero or perhaps switch signs, even between channels with the highest and lowest maximum weighting-function altitude (i.e., 6.2–10.8 μm). We propose that there is value in having more than one channel difference for inferring cloud depth, because the particular clouds being monitored in pre-CI conditions are at low altitudes initially, with inversion layers that prevent CI occurrence potentially located at any height below mid-tropospheric levels (e.g., 400 hPa).

The channel differences' trends that have no previous documented explanation or verification (via observational data or experiments), although holding significant value for estimating updraft strength—namely, the 30-min 9.7–13.4-μm trend, the 15-min 7.3–9.7-μm trend, the 15-min 6.2–7.3-μm trend, and the 30-min 6.2–7.3-μm trend (Table 7)—can be described as follows with respect to growing convective clouds: Time changes in these differences infer the rate that a convective cloud is deepening, and hence the updraft velocity (Adler and Fenn 1979; Adler et al. 1985) and the rate that a cloud is reaching altitudes where the T_B values from both channels are becoming similar. For example, 15- and 30-min trends in the 6.2–7.3-μm channel should be negative, implying that the T_B difference is becoming smaller over time as $T_{B6.2}$ nears $T_{B7.3}$.

c. Suggested implementation strategy

In this section, we propose a method for using the information provided in Tables 5–7, via a "threshold-based scoring" approach for the three main attributes of growing cumuli. This would be useful if the previously stated information was used to predict cumulus growth rates toward first-time thunderstorm occurrence via linear extrapolation of current observational trends. Table 8 lists the mean and standard deviation values for all 123 COPS events (Table 1) for the coldest pixel of the 3 × 3 box, centered over each growing cumulus in the sequence of three 15-min images (i.e., the coldest ~10%, or 1 of 9 pixels); instantaneous fields are for the last image in the three-image sequence. The list in Table 8 represents the best candidate fields for assessing cumulus cloud attributes, per category (cloud depth, cloud-top glaciation, and updraft strength). As stated previously, further testing with a full independent dataset would be needed to ascertain field importance. As a means of focusing on the growing cumulus clouds farther in advance of CI, with initial cloud-top temperatures ≥240 K, Table 9 shows fields similar to those in Table 8. Note that the rankings are somewhat different between Tables 8 and 9, suggesting field variability as clouds grow and cool, with lower averages for warmer clouds. This may be caused by the average shape of the instability profiles for the COPS data used, although more work is needed to definitively determine this conjecture.

For nowcasting CI, weighting each field along the lines of how they rank, seeking per-pixel or per–cumulus cloud object scores of 0–3, assuming normalization per physical process between 0–1, is one proposed scoring approach. Another method would be to score a cumulus

TABLE 7. As in Table 5, but the PCA of the top 8 fields that describe updraft strength in IR MSG data.

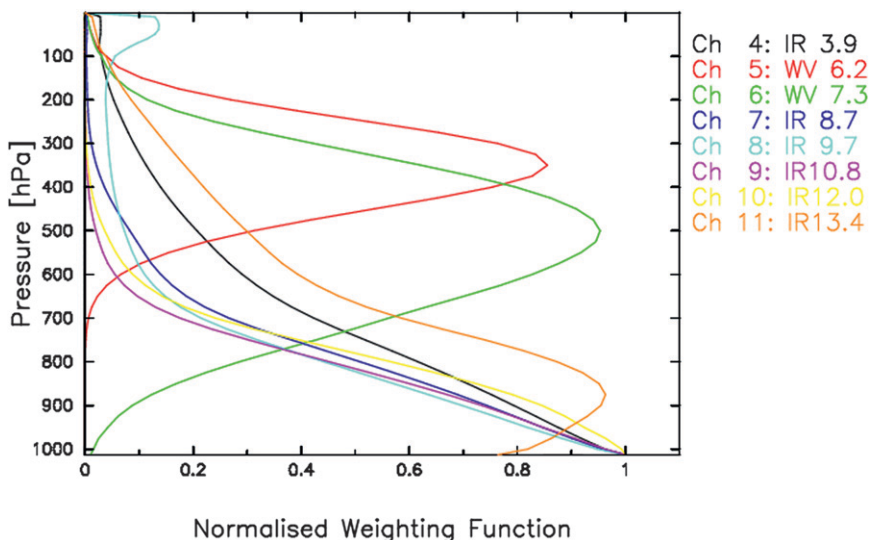| Rank	Interest fields	Component 1	Component 2	Component 3	Component 4
1	30-min 6.2–7.3 μm	0.375	−0.266	—	0.200
2	15-min 10.8-μm T_B	−0.372	−0.313	—	—
3	30-min 10.8-μm T_B	−0.370	0.343	0.172	—
4	15-min 6.2–7.3 μm	0.357	0.433	0.159	0.111
5	30-min 9.7–13.4 μm	0.354	−0.404	0.105	−0.772
6	30-min 6.2–10.8 μm	0.354	−0.175	−0.496	0.411
7	15-min 6.2–12.0 μm	0.331	0.569	−0.256	−0.302
8	15-min 7.3–9.7 μm	−0.311	—	−0.781	−0.288
	ExpVar	0.801	0.896	0.970	0.984

FIG. 3. Clear-sky per-channel SEVIRI thermal IR weighting functions as a function of altitude (see EUMETSAT 2007). Weighting functions are for SEVIRI's subsatellite point over the equator.

cloud object as 0–6 for cloud depth, 0–7 for cloud-top glaciation, and 0–8 for updraft strength. Here, normalization would not be necessary and would allow users to build scoring as a function of the thermodynamic environment in which CI was occurring and hence tailor the scoring to a given application. Another method for estimating CI likelihood for individual convective clouds is to use the mean values in Tables 8 or 9 and then defining critical values per interest field. This was the method used in the SATCAST algorithm as described previously. One strategy for estimating critical values would be to add or subtract (whichever is appropriate) ½–1 standard deviation (std dev) from the mean value, per field. For example (based on Table 8), a critical value for the 6.2–10.8-μm difference could be $-14.6 + 11.27$, or $-3.3°$, setting the 30-min 10.8-μm cloud-top cooling rate T_B to $-6.9°$ ($-20.4 + 13.54 \approx -6.9$) or setting the 8.7–10.8-μm difference to $+0.7$ [$-0.1 + (0.5 \times 1.55)$]. Depending on whether the rate of CI is important to know, these critical thresholds may be increased or decreased accordingly and, in effect, define an index along the lines of CI severity. Values in Table 9 may be considered for clouds in warmer environments or where the instability is relatively low.

Because convective environments (or convective regimes; Boccippio et al. 2005; Cecil et al. 2005; Li et al. 2006) vary considerably one needs to be conscious of the fact that growing cumulus clouds will exhibit different cloud-top signals in terms of emitted radiance across the IR spectrum. This is caused by 1) variation in integrated moisture, or precipitable water (PW), and water vapor amounts, which influence the altitude of maximum

weighting function response; 2) the local freezing altitude, which impacts cloud-top glaciation rates and to some extent updraft characteristics as a function of altitude via latent heat releases from condensation and

TABLE 8. Mean and std dev values for the interest fields in Tables 5–7. These fields are grouped by category as they pertain to estimating cloud depth, cloud-top glaciation, and updraft strength. Fields are listed by order of the ranking as shown in Tables 5–7.

Rank	CI interest fields	Mean (K)	Std dev (K)
Cloud depth			
1	6.2–10.8 μm	−14.6	11.27
2	6.2–7.3 μm	−6.6	5.94
3	10.8-μm T_B	242.5	16.79
4	7.3–13.4 μm	5.4	4.42
5	6.2–9.7 μm	−8.4	3.40
6	8.7–12.0 μm	0.3	1.92
Glaciation indicators			
1	15-min tripectral	0.7	2.02
2	Trispectral	−0.6	1.94
3	15-min 8.7–10.8 μm	0.5	1.47
4	8.7–10.8 μm	−0.1	1.55
5	15-min 12.0–10.8 μm	0.2	1.05
6	15-min 3.9–10.8 μm	0.3	0.24
7	12.0–10.8 μm	−0.5	1.15
Updraft strength			
1	30-min 6.2–7.3 μm	7.2	4.92
2	15-min 10.8-μm T_B	−12.1	9.44
3	30-min 10.8-μm T_B	−20.4	13.54
4	15-min 6.2–7.3 μm	4.3	3.58
5	30-min 9.7–13.4 μm	4.9	4.31
6	30-min 6.2–10.8 μm	14.5	8.78
7	15-min 6.2–12.0 μm	8.0	6.32
8	15-min 7.3–9.7 μm	−3.3	4.02

TABLE 9. As in Table 8, but for clouds with cloud-top temperatures ≥240 K. These fields are again grouped by category. Note that the rankings determined from PCA have changed somewhat compared to those in Tables 5–7, suggesting field variability as clouds grow and cool in this warmer subset of clouds.

Rank	CI interest fields	Mean (K)	Std dev (K)
Cloud depth			
1	6.2–10.8 μm	−23.4	7.94
2	10.8-μm T_B	256.3	9.20
3	6.2–7.3 μm	−11.3	3.86
4	7.3–13.4 μm	3.5	4.09
5	6.2–9.7 μm	−9.11	3.85
6	8.7–12.0 μm	0.3	2.32
Glaciation indicators			
1	8.7–10.8 μm	−0.6	1.58
2	15-min 8.7–10.8 μm	0.6	1.26
3	15-min trispectral	0.6	1.31
4	Trispectral	−1.5	1.46
5	15-min 3.9–10.8 μm	0.2	0.23
6	12.0–10.8 μm	−0.9	1.12
7	15-min 12.0–10.8 μm	−0.2	0.93
Updraft strength			
1	30-min 6.2–7.3 μm	4.4	3.79
2	30-min 10.8-μm T_B	−12.4	9.96
3	15-min 6.2–7.3 μm	2.9	3.13
4	15-min 10.8-μm T_B	−7.4	7.53
5	30-min 6.2–10.8 μm	10.9	8.18
6	15-min 6.2–12.0 μm	6.4	6.77
7	30-min 9.7–13.4 μm	2.3	3.18
8	15-min 7.3–9.7 μm	−0.6	2.12

freezing; 3) instability, the amount of convective available potential energy and its vertical profile, which impacts updraft velocity directly and indirectly the spectral signature of glaciation via cloud-top microphysics (e.g., Rosenfeld et al. 2008; Lensky and Rosenfeld 2008); and 4) the depth of the boundary layer and cloud-base heights, which influence updraft width and hence strength (Williams et al. 2005). Therefore, with background knowledge of the convective environment comes an understanding of how to implement the interest fields, especially related to the physical attributes and processes of the cumulus convection being monitored. Background information can come from NWP model grids [e.g., the European Centre for Medium Range Weather Forecasting (ECMWF)] or other satellite remote sensing retrievals (in the case of PW). As a result of variations in the convective environment, the suggested implementation strategy here will need to be used as a first guess, with subsequent adjustments needed to determine each field's "critical threshold" for optimally identifying CI. Development of a probabilistic approach to nowcasting CI using IR fields is in the future and implies that IR field–environment relationships are well understood.

d. Error sources

The main sources of error in this study are summarized. First, because the CI events used in this study were determined subjectively, it is likely that several of the 123 cases are not ideally oriented in time and space relative to the *Meteosat-9* data used. Specifically, it is possible that at the initial time (of the sequence of three 15-min images) the clouds may have already reached the "towering" cumulus stage. The goal was to capture cumuli in the mediocris (moderate) stage, just beyond the "fair weather" stage, at the initial time (as exemplified in Fig. 1a). Therefore, by the third image in the sequence (e.g., cumulonimbus calvus), CI may nearly be occurring. The physical processes of growing cumuli related to the *Meteosat-9* data should, however, still be captured. A second and related source of error is that the subjective determination of cumulus cloud types in a three-image sequence at times is likely occasionally incorrect. This is caused by challenges involved in identifying cumulus in 1-km HRV and 3-km IR sampling distance pixels (actual IR resolution over the COPS region was nearer 4 km because of the view angle). View angle influences over the COPS domain, being poleward of 46.5°, cause difficulty in interpreting cloud types from satellite, which again likely lead to some false determination of the size or type of pre-CI convective clouds. Also, at these latitudes, SEVIRI observes both cloud sides and tops simultaneously in a given cumulus cloud pixel, which will dull pure cloud-top signatures (as used in channel differencing approaches). View angle effects also vary spectrally, with channels like 9.7 and 13.4 μm influenced more than the 3.9- and 10.8-μm data. This will also contribute to problems with any simple differencing technique. A third main source of error is the likelihood that higher-level cirrus clouds obscured lower cumulus clouds in some of the images, which will negatively affect the observed IR signatures by cooling channel T_B.

Other more minor sources of error include the following: 1) the occasional inadequate observation of a given new thunderstorm development by COPS ground-based radar and that, for some CI events, the 15-min MSG data were of too low temporal resolution to measure cloud-top features at times consistent with optimally describing the three attributes of convective clouds being analyzed (Schmit et al. 2009); 2) it is quite possible that some CI events used in the study never achieved >35-dBZ echo intensity; and 3) registration and navigation issues will likely cause per-storm channel difference errors, although these problems are expected to be small with SEVIRI (<1 km; Schmetz et al. 2002).

Despite these errors, it is because of the large sample size (123 events) that most of the main statistical signals

are well represented. This is exemplified in Tables 8 and 9 with reasonable statistics that show expected variability via the standard deviation calculations.

5. Conclusions

A total of 67 SEVIRI IR CI interest fields are initially assessed for containing information on three attributes of growing convective clouds: cloud depth, updraft strength, and cloud-top glaciation. Through correlation and principal component analyses, 21 out of the 67 fields are identified as containing the least amount of redundant information. Using between six and eight fields per category, two methods are proposed on how growing convective clouds may be quantified per MSG pixel (with 3-km scaling distance), or per cumulus cloud "object," toward monitoring cumulus cloud development.

An important aspect of this research comes when one looks into the near future of geostationary meteorological satellite technology over North America, specifically for the forthcoming Advanced Baseline Imager (ABI), which will be aboard the GOES-R series of satellites. ABI is expected to possess near-IR and IR channels (central wavelengths at 1.61, 3.9, 6.15, 7.0, 8.5, 10.35, 11.2, 12.3, and 13.3 μm; National Oceanic and Atmospheric Administration National Environmental Satellite, Data, and Information Service). Therefore, the results developed here for SEVIRI will be immediately useful to ABI for applications related to CI nowcasting and the monitoring of growing, evolving cumulus clouds prior to thunderstorm development. Furthermore, these results should help to better define how multichannel IR data can be used within thunderstorm nowcast systems such as SATCAST, the Corridor Integrated Weather System (CIWS; Wolfson and Clark 2006), the Thunderstorm Identification, Tracking, and Nowcasting (TITAN; Han et al. 2009), Cumulonim Bus Tracking and Monitoring (Cb-TRAM; Zinner et al. 2008), and those as reviewed in Wilson et al. (2004).

Future work beyond this study will involve testing the previous results within an algorithm that monitors convective clouds over time or within a CI nowcast system as listed earlier. These validation efforts will include the assessment of a wide range of cases, especially null events where cumulus clouds evolved as predicted by IR interest field observations but rainfall never reaches a critical intensity (i.e., a thunderstorm never developed). The study by Siewert et al. (2010) represents one preliminary testing and validation effort. Such work will allow for an estimation of the field importance (per cloud attribute) as a function of convective environment, allowing interest field thresholds to be adjusted as a function of space and time, based on background knowledge. For example, given the knowledge of the lifted condensation level (using near-surface temperature and dewpoint), a better estimate of cloud-top height (and hence a much better evaluation of actual cloud depth) may be obtained. Similarly, knowledge of the freezing level and PW will help to determine optimal cloud-top glaciation indicators, given the variability in the channel weighting function structure with height.

REFERENCES

Ackerman, S. A., 1996: Global satellite observations of negative brightness temperature differences between 11 and 6.7 μm. *J. Atmos. Sci.,* **53,** 2803–2812.

——, R. A. Frey, and W. L. Smith, 1992: Radiation budget studies using collocated observations from AVHRR, HIRS/2, and ERBE instruments. *J. Geophys. Res.,* **97,** 11 513–11 525.

Adler, R. F., and D. D. Fenn, 1979: Thunderstorm intensity as determined from satellite data. *J. Appl. Meteor.,* **18,** 502–517.

——, M. J. Markus, and D. D. Fenn, 1985: Detection of severe Midwest thunderstorms using geosynchronous satellite data. *Mon. Wea. Rev.,* **113,** 769–781.

Balaji, V., and T. L. Clark, 1988: Scale selection in locally forced convective fields and the initiation of deep cumulus. *J. Atmos. Sci.,* **45,** 3188–3211.

Baum, B. A., and J. D. Spinhirne, 2000: Remote sensing of cloud properties using MODIS airborne simulator imagery during SUCCESS. 3. Cloud overlap. *J. Geophys. Res.,* **105** (D9), 11 793–11 804.

——, V. Tovinkere, J. Titlow, and R. M. Welch, 1997: Automated cloud classification of global AVHRR data using a fuzzy logic approach. *J. Appl. Meteor.,* **36,** 1519–1540.

——, D. P. Kratz, P. Yang, S. Ou, Y. Hu, P. F. Soulen, and S.-C. Tsay, 2000a: Remote sensing of cloud properties using MODIS airborne simulator imagery during SUCCESS. 1. Data and models. *J. Geophys. Res.,* **105** (D9), 11 767–11 780.

——, P. F. Soulen, K. I. Strabala, M. D. King, S. A. Ackerman, W. P. Menzel, and P. Yang, 2000b: Remote sensing of cloud properties using MODIS airborne simulator imagery during SUCCESS. 2. Cloud thermodynamic phase. *J. Geophys. Res.,* **105** (D5), 11 781–11 792.

Berendes, T. A., K. S. Kuo, A. M. Logar, E. M. Corwin, R. M. Welch, B. A. Baum, A. Pretre, and R. C. Weger, 1999: A comparison of paired histogram, maximum likelihood, class elimination, and neural network approaches for daylight global cloud classification using AVHRR imagery. *J. Geophys. Res.,* **104** (D6), 6199–6213.

——, J. R. Mecikalski, W. M. Mackenzie, K. M. Bedka, and U. S. Nair, 2008: Convective cloud detection in satellite imagery using standard deviation limited adaptive clustering. *J. Geophys. Res.,* **113,** D20207, doi:10.1029/2008JD010287.

Bethwaite, F. D., E. J. Smith, J. A. Warburton, and H. Heffernan, 1966: Effects of seeding isolated cumulus clouds with silver iodide. *J. Appl. Meteor.,* **5,** 513–520.

Boccippio, D. J., W. A. Petersen, and D. J. Cecil, 2005: The tropical convective spectrum. Part I: Archetypal vertical structures. *J. Climate,* **18,** 2744–2769.

Browning, K. A., 1982: *Nowcasting.* Academic Press. 256 pp.

——, and D. Atlas, 1965: Initiation of precipitation in vigorous convective clouds. *J. Atmos. Sci.,* **22,** 678–683.

Brunner, J. C., S. A. Ackerman, A. S. Bachmeier, and R. M. Rabin, 2007: A quantitative analysis of the enhanced-V feature in relation to severe weather. *Wea. Forecasting,* **22,** 853–872.

Cecil, D. J., S. J. Goodman, D. J. Boccippio, E. J. Zipser, and S. W. Nesbitt, 2005: Three years of TRMM precipitation features. Part I: Radar, radiometric, and lightning characteristics. *Mon. Wea. Rev.,* **133,** 543–566.

Ellrod, G. P., 1995: Advances in the detection and analysis of fog at night using GOES multispectral infrared imagery. *Wea. Forecasting,* **10,** 606–619.

——, 2004: Impact of volcanic ash detection caused by the loss of the 12 μm "split window" band on GOES-M imagers. *J. Volcanol. Geotherm. Res.,* **135** (1–2), 91–103.

EUMETSAT, 2007: MSG Level 1.5 image data format description. Document number EUM/MSG/ICD/105, 122 pp. [Available online at http://www.eumetsat.int/groups/ops/documents/document/pdf_ten_05105_msg_img_data.pdf.]

Goloub, P., M. Herman, H. Chepfer, J. Riedi, G. Brogniez, P. Couvert, and G. Séze, 2000: Cloud thermodynamical phase classification from the POLDER spaceborne instrument. *J. Geophys. Res.,* **105** (D11), 14 747–14 759.

Han, L., Y. Zheng, H. Wang, and Y. Lin, 2009: 3D convective storm identification, tracking, and forecasting—An enhanced TITAN algorithm. *J. Atmos. Oceanic Technol.,* **26,** 719–732.

Holz, R. E., S. Ackerman, P. Antonelli, F. Nagle, R. O. Knuteson, M. McGill, D. L. Hlavka, and W. D. Hart, 2006: An improvement to the high-spectral-resolution CO_2-slicing cloud-top altitude retrieval. *J. Atmos. Oceanic Technol.,* **23,** 653–670.

Inoue, T., 1987a: A cloud type classification with NOAA-7 split-window measurements. *J. Geophys. Res.,* **92** (D4), 3991–4000.

——, 1987b: An instantaneous delineation of convective rainfall area using split window data of NOAA-7 AVHRR. *J. Meteor. Soc. Japan,* **65,** 469–481.

Jacobs, A. J. M., and N. Maat, 2005: Numerical guidance methods for decision support in aviation meteorological forecasting. *Wea. Forecasting,* **20,** 82–100.

Johnson, R. A., and D. W. Wichern, 2002: *Applied Multivariate Statistical Analysis.* 5th ed. Prentice Hall, 767 pp.

Lensky, I. M., and D. Rosenfeld, 2008: Clouds-Aerosols-Precipitation Satellite Analysis Tool (CAPSAT). *Atmos. Chem. Phys.,* **8,** 6739–6753.

Levizzani, V., and M. Setvák, 1996: Multispectral, high-resolution satellite observations of plumes on top of convective storms. *J. Atmos. Sci.,* **53,** 361–369.

Li, X., S. Zhang, and D.-L. Zhang, 2006: Thermodynamic, cloud microphysics, and rainfall responses to initial moisture perturbations in the tropical deep convective regime. *J. Geophys. Res.,* **111,** D14207, doi:10.1029/2005JD006968.

Lindsey, D. T., D. W. Hillger, L. Grasso, J. A. Knaff, and J. F. Dostalek, 2006: GOES climatology and analysis of thunder-

storms with enhanced 3.9-μm reflectivity. *Mon. Wea. Rev.,* **134,** 2342–2353.

McCann, D. W., 1983: The enhanced-V: A satellite observable severe storm signature. *Mon. Wea. Rev.,* **111,** 887–894.

Mecikalski, J. R., and K. M. Bedka, 2006: Forecasting convective initiation by monitoring the evolution of moving cumulus in daytime GOES imagery. *Mon. Wea. Rev.,* **134,** 49–78.

——, and Coauthors, 2007: Aviation applications for satellite-based observations of cloud properties, convective initiation, in-flight icing, turbulence and volcanic ash. *Bull. Amer. Meteor. Soc.,* **88,** 1589–1607.

——, K. M. Bedka, S. J. Paech, and L. A. Litten, 2008: A statistical evaluation of GOES cloud-top properties for predicting convective initiation. *Mon. Wea. Rev.,* **136,** 4899–4914.

Menzel, W. P., F. C. Holt, T. J. Schmit, R. M. Aune, A. J. Schreiner, and D. G. Gray, 1998: Application of *GOES 8/9* soundings to weather forecasting and nowcasting. *Bull. Amer. Meteor. Soc.,* **79,** 2059–2077.

Mueller, C. K., J. W. Wilson, and N. A. Crook, 1993: The utility of sounding and mesonet data to nowcast thunderstorm initiation. *Wea. Forecasting,* **8,** 132–146.

——, T. Saxen, R. Roberts, J. Wilson, T. Betancourt, S. Dettling, N. Oien, and J. Yee, 2003: NCAR auto-nowcast system. *Wea. Forecasting,* **18,** 545–561.

Nair, U. S., R. C. Weger, K. S. Kuo, and R. M. Welch, 1998: Clustering, randomness, and regularity in cloud fields 5. The nature of regular cumulus cloud fields. *J. Geophys. Res.,* **103,** 11 363–11 380.

Pavolonis, M. J., W. F. Feltz, A. K. Heidinger, and G. M. Gallina, 2006: A daytime complement to the reverse absorption technique for improved automated detection of volcanic ash. *J. Atmos. Oceanic Technol.,* **23,** 1422–1444.

Prata, A. J., 1989: Observations of volcanic ash clouds in the 10–12 μm window using AVHRR/2 data. *Int. J. Remote Sens.,* **10,** 751–761.

Purdom, J. F. W., 1976: Some uses of high resolution GOES imagery in the mesoscale forecasting of convection and its behavior. *Mon. Wea. Rev.,* **104,** 1474–1483.

——, 1982: Subjective interpretations of geostationary satellite data for nowcasting. *Nowcasting,* K. Browning, Ed. Academic Press, 149–166.

Rickenbach, T., P. Kucera, M. Gentry, L. Carey, A. Lare, R. F. Lin, B. Demoz, and D. O. Starr, 2008: The relationship between anvil clouds and convective cells: A case study in South Florida during CRYSTAL-FACE. *Mon. Wea. Rev.,* **136,** 3917–3932.

Roberts, R. D., and S. Rutledge, 2003: Nowcasting storm initiation and growth using GOES-8 and WSR-88D data. *Wea. Forecasting,* **18,** 562–584.

Rosenfeld, D., W. L. Woodley, A. Lerner, G. Kelman, and D. T. Lindsey, 2008: Satellite detection of severe convective storms by their retrieved vertical profiles of cloud particle effective radius and thermodynamic phase. *J. Geophys. Res.,* **113,** D04208, doi:10.1029/2007JD008600.

Rozumalski, R. A., 2000: A quantitative assessment of the NESDIS auto-estimator. *Wea. Forecasting,* **15,** 397–415.

Sadler, J. C., and B. Kilonsky, 1985: Deriving surface winds from satellite observations of low-level cloud motions. *J. Climate Appl. Meteor.,* **24,** 758–769.

Schmetz, J., S. A. Tjemkes, M. Gube, and L. van de Berg, 1997: Monitoring deep convection and convective overshooting with METEOSAT. *Adv. Space Res.,* **19,** 433–441.

——, P. Pili, S. Tjemkes, D. Just, J. Kerkmann, S. Rota, and A. Ratier, 2002: An introduction to Meteosat Second Generation (MSG). *Bull. Amer. Meteor. Soc.,* **83,** 977–992.

Schmit, T. J., J. Li, S. A. Ackerman, and J. J. Gurka, 2009: High spectral- and high-temporal-resolution infrared measurements from geostationary orbit. *J. Atmos. Oceanic Technol.,* **26,** 2273–2292.

Scofield, R. A., 1987: The NESDIS operational convective precipitation technique. *Mon. Wea. Rev.,* **115,** 1773–1792.

Setvák, M., R. M. Rabin, C. A. Doswell, and V. Levizzani, 2003: Satellite observations of convective storm top features in the 1.6 and 3.7/3.9 μm spectral bands. *Atmos. Res.,* **67–68C,** 589–605.

Siewert, C. W., M. Koenig, and J. R. Mecikalski, 2010: Application of Meteosat Second Generation data towards improving the nowcasting of convective initiation. *Meteor. Appl.,* in press.

Strabala, K. I., S. A. Ackerman, and W. P. Menzel, 1994: Cloud properties inferred from 8–12 μm data. *J. Appl. Meteor.,* **33,** 212–229.

Velden, C. S., C. M. Hayden, S. J. Nieman, W. P. Menzel, S. Wanzong, and J. S. Goerss, 1997: Upper-tropospheric winds derived from geostationary satellite water vapor observations. *Bull. Amer. Meteor. Soc.,* **78,** 173–195.

Weckwerth, T. M., and D. B. Parsons, 2006: A review of convection initiation and motivation for IHOP_2002. *Mon. Wea. Rev.,* **134,** 5–22.

Williams, E., V. Mushtak, D. Rosenfeld, S. Goodman, and D. Boccippio, 2005: Thermodynamic conditions favorable to superlative thunderstorm updraft, mixed phase microphysics and lightning flash rate. *Atmos. Res.,* **76,** 288–306.

Wilson, J. W., N. A. Crook, C. K. Mueller, J. Sun, and M. Dixon, 1998: Nowcasting thunderstorms: A status report. *Bull. Amer. Meteor. Soc.,* **79,** 2079–2099.

——, E. E. Ebert, T. R. Saxen, R. D. Roberts, C. K. Mueller, M. Sleigh, C. E. Pierce, and A. Seed, 2004: Sydney 2000 forecast demonstration project: Convective storm nowcasting. *Wea. Forecasting,* **19,** 131–150.

Wolfson, M. M., and D. A. Clark, 2006: Advanced aviation weather forecasts. *MIT Lincoln Lab. J.,* **16.** [Available online at http://www.ll.mit.edu/publications/journal/pdf/vol16_no1/16_1_3Wolfson.pdf.]

Wulfmeyer, V., and Coauthors, 2008: RESEARCH CAMPAIGN: The Convective and Orographically Induced Precipitation Study. *Bull. Amer. Meteor. Soc.,* **89,** 1477–1486.

Zhang, F., A. M. Odins, and J. W. Nielsen-Gammon, 2006: Mesoscale predictability of an extreme warm-season precipitation event. *Wea. Forecasting,* **21,** 149–166.

Ziegler, C. L., T. J. Lee, and R. A. Pielke, 1997: Convective initiation at the dryline: A modeling study. *Mon. Wea. Rev.,* **125,** 1001–1026.

Zinner, T., H. Mannstein, and A. Tafferner, 2008: Cb-TRAM: Tracking and monitoring severe convection from onset over rapid development to mature phase using multi-channel *Meteosat-8* SEVIRI data. *Meteor. Atmos. Phys.,* **101,** 191–210.